# A Grid-Refinement-Based Approach for Modeling the Convective Boundary Layer in the Gray Zone: A Pilot Study

BOWEN ZHOU

*Key Laboratory for Mesoscale Severe Weather, Ministry of Education, and School of Atmospheric Sciences, Nanjing University, Nanjing, China*

MING XUE

*Key Laboratory for Mesoscale Severe Weather, Ministry of Education, and School of Atmospheric Sciences, Nanjing University, Nanjing, China, and Center for Analysis and Prediction of Storms, and School of Meteorology, University of Oklahoma, Norman, Oklahoma*

KEFENG ZHU

*Key Laboratory for Mesoscale Severe Weather, Ministry of Education, and School of Atmospheric Sciences, Nanjing University, Nanjing, China*

(Manuscript received 4 January 2017, in final form 14 June 2017)

ABSTRACT

The model gray zone refers to the range of grid spacings comparable to the dominant length scale of the flow. In the gray zone, the flow is partially resolved and partially subgrid scale (SGS). Neither ensemble-averaging-based parameterizations nor turbulence closures are appropriate for parameterizing the effects of SGS motions on the resolved flow. The gray zone of the convective boundary layer (CBL) is in the range of CBL depth, typically $O(1)$ km. A new approach that seeks explicit resolution of the unstable surface layer through a nest layer of fine grid spacing is proposed to improve CBL parameterization in the gray zone. To provide the theoretical basis for the approach, a linear analytic model is presented, and one-way nested simulations are performed to investigate the dynamical coupling between the surface layer and the mixed layer. The analytic model shows that at the onset of thermal instability, the vertical and horizontal structures of the mixed layer are set by surface-layer forcings. The nested 3D simulations extend the findings from the analytic model and further reveal potential improvements in high-order statistics and resolved convective structures both including and extending above the nest region compared to the stand-alone gray-zone simulations. This study suggests that when the most energetic scales of CBL convection are resolved in the surface layer, the overall simulation of the CBL improves at gray-zone resolutions.

## 1. Introduction

In the daytime convective boundary layer (CBL), the boundary layer depth $z_i$ represents the characteristic length scale of organized convective circulations (Lenschow and Stankov 1986). For typical daytime conditions over land, $z_i$ can grow to about 1–2 km (Kaimal and Finnigan 1994). In numerical models with grid spacing $\Delta_g \gg z_i$, such as in mesoscale and general circulation models, CBL turbulence is represented entirely by planetary boundary layer (PBL) schemes. When $\Delta_g \ll z_i$, such as in high-resolution cloud-resolving models and large-eddy simulations (LESs), CBL turbulence is mostly resolved, while the sub-grid-scale (SGS) fluctuations are represented by turbulence closures. When $\Delta_g$ is comparable to $z_i$, neither PBL schemes nor turbulence closures are appropriate. This range of $\Delta_g$ is named *terra incognita* by Wyngaard (2004) and is also widely known as the model gray zone (Arakawa et al. 2011; Arakawa and Wu 2013). It describes the situation where the scale of the spatial filter, or loosely speaking, the model grid spacing, is comparable to the characteristic length scale of the flow. In the model gray zone, neither ensemble-averaging-based parameterizations nor turbulence closures are appropriate. For the CBL, the lack

*Corresponding author*: Bowen Zhou, zhoubowen@nju.edu.cn

DOI: 10.1175/JAS-D-16-0376.1

of applicable SGS parameterization in the grid-spacing range of $z_i$ presents a challenge to modern-day numerical weather prediction (NWP) models, whose spatial resolutions are rapidly approaching ~1-km scale (Xue et al. 2013). Another application that often traverses the CBL gray-zone scales is regional dynamical downscaling via grid nesting (e.g., Mirocha et al. 2013; Muñoz-Esparza et al. 2017).

If sufficient computational resources and highly scalable NWP models allow, the PBL gray zone can be avoided by increasing the grid resolution to be at least an order of magnitude finer than $z_i$.[1] Currently, typical resolutions of operational NWP models are between a few and 10 km or so (Xue et al. 2013). If the horizontal grid resolutions were to increase from $O(10)$ km to $O(100)$ m, thus avoiding the CBL gray zone, the computational cost would likely increase by more than a million times.[2] In addition, dodging the gray zone is futile since atmospheric flows are inherently multiscale. The next gray zone, such as gravity waves having wavelengths of a few hundred meters (Newsom and Banta 2003) or nighttime stable boundary layer flows with buoyancy length scales $O(10)$ m (Stull 1988, chapter 12), will keep on emerging.

Quite a few studies have exposed issues of gray-zone CBL modeling with either turbulence closures or PBL schemes. When simulating an idealized CBL, Xue et al. (1996) found that the 1.5-order turbulence kinetic energy (TKE)-based SGS turbulence closure of Deardorff (1974) operating on the order of 1-km horizontal grid spacing lacks vertical mixing, such that the potential temperature profile is superadiabatic throughout the depth of the CBL. LeMone et al. (2010) simulated a fair-weather CBL with the Yonsei University (YSU) PBL scheme (Hong et al. 2006). They found that when horizontal grid resolution is decreased from 1 km to 200 m, convective organization changed from linear rolls to broken cells. Gibbs et al. (2011) evaluated model predictions of turbulent flow parameters in a dry CBL. For all three PBL schemes tested, they found similar convection structures for 4, 2, and 1 km horizontal grid spacings and concluded that the value added through refining grid spacing from 4 to 1 km was minimal. Potential problems with gray-zone modeling could further affect derivative applications of NWP such as air quality modeling (Ching et al. 2014, hereafter C14) and fire danger forecasting (Thurston et al. 2016).

Several scale-aware gray-zone PBL schemes have emerged in recent years by introducing the horizontal grid spacing $\Delta_g$ as an additional variable to existing PBL schemes. First, the variation of SGS fluxes as a function of the dimensionless grid spacing $\Delta_g/z_i$ is determined empirically by coarse graining idealized CBLs simulated by LESs (e.g., Honnert et al. 2011; Shin and Hong 2013; Malavelle et al. 2014),

$$\overline{w'\varphi'}^{\mathrm{SGS}}(\Delta_g) = f_\varphi\left(\frac{\Delta_g}{z_i}\right)\overline{w'\varphi'}^{\mathrm{PBL}}, \qquad (1)$$

where $\overline{w'\varphi'}^{\mathrm{SGS}}$ and $\overline{w'\varphi'}^{\mathrm{PBL}}$ are the SGS and total turbulent fluxes of variable $\varphi$. The latter is obtained from the original PBL scheme. The $f_\varphi$ defines the SGS partition of $\overline{w'\varphi'}$ for different $\Delta_g/z_i$ across the gray zone and usually differs for different values of $\varphi$; $f_\varphi$ approaches unity at mesoscale spacings ($\Delta_g/z_i \gg 1$) and restores to the original PBL scheme. It decreases monotonically as resolution refines and diminishes at LES spacings where turbulence is well resolved.

Scale-aware PBL schemes are built upon these predetermined empirical partition functions $f_\varphi$ to regulate the amount of fluxes produced by the original PBL scheme for a particular $\Delta_g$. Examples include Boutle et al. (2014)'s adaption of the Lock et al. (2000) scheme and Shin and Hong (2015)'s adaption of the YSU scheme. Modification of the Mellor–Yamada–Nakanishi–Niino (MYNN) model (Nakanishi and Niino 2009) by Ito et al. (2015) was more subtle, where the empirical partition function was not applied directly to the fluxes but to the dissipation length in the TKE equation. Efstathiou et al. (2016) combined the Boutle et al. (2014) scheme with the 3D Smagorinsky LES closure to create a so-called blending scheme that allows a smooth transition from PBL schemes to turbulence closures.

While flux-partition functions allow practical extensions of PBL schemes into the gray zone, their physical basis as well as their universality still remains unclear. The main objective of this paper is to examine the possibility of a generic approach for improving CBL parameterization in the gray zone. It is based on the physical understanding of gray-zone convection as explained in C14 and Zhou et al. (2014, hereafter ZSC14). The proposed method is through horizontal grid refinement and two-way interactive vertical grid nesting. This study provides the theoretical basis and

[1] Skamarock (2004) found that the effective resolution of the WRF Model, one of the most widely used NWP models, occurs between 6 and 8$\Delta_g$ as opposed to the 2$\Delta_g$ Nyquist cutoff (minimum resolvable) length scale. However, Sullivan and Patton (2011) suggested that higher-order PBL statistics and turbulence spectra converge only at $z_i/\Delta_g$ greater than 60.

[2] There would be 100 × 100 times more grid points in the horizontal directions and about 100-times-finer time steps due to the Courant condition. Switching from highly efficient one-dimensional (1D; single column) PBL schemes to 3D turbulence closures incurs additional computational cost.

proves the feasibility of the proposed approach. The implementation and results of the new approach are presented in a separate paper.

## 2. A grid-refinement-based approach

The classic CBL driven by surface heating can be divided into three vertical layers (Stull 1988) as illustrated in Fig. 1. The potential temperature Θ profile outlines the stability of the CBL at different heights. The surface layer in the bottom 10%–15% is superadiabatic, the mixed layer in the middle is near neutral, and the entrainment zone in the top 10%–20% is stably stratified. Thermal instability originates from the unstable surface layer and quickly propagates to the entire CBL. Convective organizations are largely set by the intrinsic thermal instability of the CBL while influenced by vertical wind shear (Salesky et al. 2017).

When the grid spacing $\Delta_g$ of a mesoscale model is refined to the gray-zone range, spurious resolved convection sets in from the surface layer (C14; ZSC14). The onset of resolved convection can be predicted through a grid-dependent critical turbulent Rayleigh number $\mathrm{Ra}(\Delta_g/z_i)$ based on the unstable surface-layer depth. As shown in ZSC14, for typical mesoscale grid spacings, $\mathrm{Ra}(\Delta_g/z_i)$ is too large to be achievable throughout daytime, such that no resolved convection can ever occur. When $\Delta_g/z_i$ approaches unity, $\mathrm{Ra}(\Delta_g/z_i)$ is rapidly lowered. When Ra is exceeded some time during the day, that is, when eddy diffusivity is no longer sufficient to mix heat upward, spurious resolved convection initiates. The resulting convective structures are much broader than $z_i$ in terms of size and are also overly energetic. The spurious resolved convection not only degrades the quality of the simulated CBL but may also distort other resolvable flow features (see the lake breeze example in C14).

Given the importance of the surface layer on controlling the onset of thermal instability in the CBL, C14 sets a limit on Ra so that spurious resolved convection is altogether suppressed. This is done by increasing eddy diffusivity in the surface layer, thus lowering Ra below its critical value. The method of C14 is universally applicable to eddy-diffusion-based PBL schemes. Once applied, it effectively nudges the gray-zone solution toward a mesoscale one. In terms of CBL dynamics, refinement of grid resolution into the gray zone has little added value since it does not resolve any more scales than on a mesoscale grid. However, C14 shows that elimination of spurious convection allows coexisting flow of other scales (such as the lake breeze example in their study) to be properly resolved.

Instead of quenching resolved convection in the surface layer as in C14, if we could resolve surface-layer

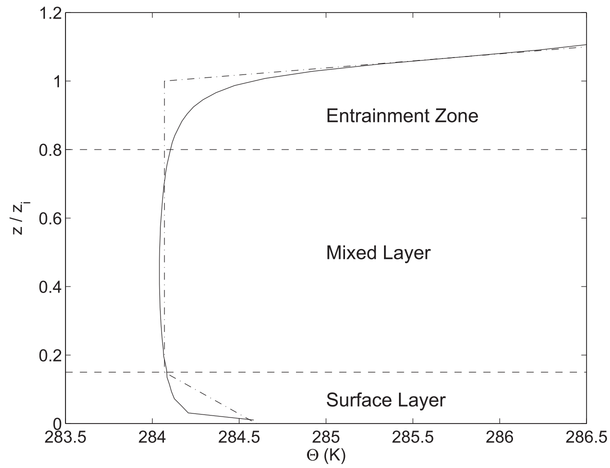


FIG. 1. Schematic of the potential temperature profile in the CBL driven by surface heating. The solid curve is from a high-resolution LES of the Wangara CBL at local noon. The LES has 25-m isotropic grid spacing and 1248 × 1248 × 100 grid points; see ZSC14 for details. The dash–dotted curve is a piecewise linear approximation. The magnitude of Θ is specific to the Wangara case and not universal.

instability properly, the overall CBL simulation would improve in terms of the onset timing of resolved convection and the dominant instability length scale (i.e., the size of the convective structures). To resolve the most energetic scales of motion in the surface layer, finer resolution is certainly required. But instead of refining grid resolution for the whole model domain, we propose to refine the grid resolution of the surface layer only while keeping the original grid for the rest of the model to save computational cost. This can be done by vertically nesting a layer of fine-resolution grid inside the parent grid. A 2D schematic of the grid setup is presented in Fig. 2. The nest grid extends from vertical level 1 to $n_z$. The rest of the parent grid from vertical level $n_{z+1}$ to $N_z$ remains unchanged. The horizontal grid spacings of nest grid and parent are $\delta_{x,y}$ and $\Delta_{x,y}$, respectively. The vertical grid spacing $\Delta_z$ is identical for both grids. Vertical grid refinement in the nest grid is not necessary since $\Delta_z$, usually around 50 m or finer with grid stretching, is already much finer than $\Delta_{x,y}$, which is the primary limiting factor in resolving CBL convection. Lateral boundaries of the two grids overlap. SGS turbulent mixing in the fine nest and coarse parent grids are parameterized by an LES turbulence closure and a PBL scheme, respectively. The parent and nest grids communicate through two-way interactive nesting.

In theory, the method is advantageous over the flux-partition-correction approach, because it is developed in response to CBL dynamics in the gray zone. It does not rely on predetermined empirical functions to introduce grid (scale) dependency, so it should be

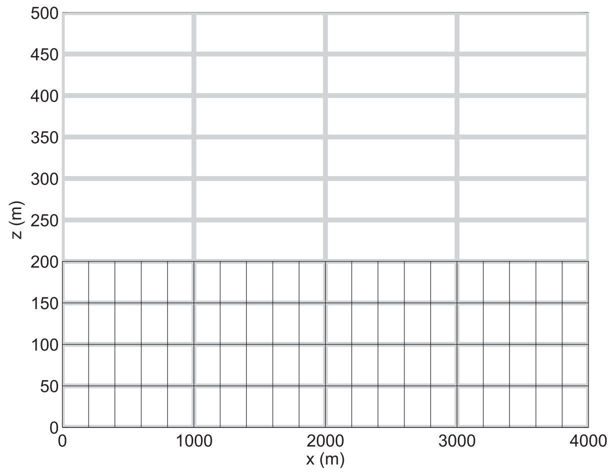


FIG. 2. A 2D schematic of the vertically nested gray-zone grid. Thick gray lines and thin black lines represent the coarse and fine grids, respectively. The horizontal spacings are 1000 and 200 m for the parent and nest grids, respectively, with a refinement ratio of 5. The vertical spacing is 50 m. The nest grid occupies the bottom five levels.

universally applicable to any PBL scheme. The computational cost is expected to be higher than flux-partition methods. However, it can be kept under achievable limits since the surface layer is only 10%–15% of the CBL, 1% of the troposphere. In terms of vertical grid points, the surface layer usually occupies no more than 10% of a typical mesoscale model column.

Before implementation, the theoretical basis for the proposed approach must be established. Specifically, the dynamic coupling between convection within and above the surface layer must be determined. For the grid-refinement-based method to work, resolved convection above the surface layer must respond to surface-layer forcings and conform to the convective structures set by the surface-layer instability. This cannot be assumed a priori for turbulent convection. For example, Sullivan et al. (1996) found that small-scale surface-layer turbulence tends to stay within the surface layer. When they applied a two-way nested grid in an LES to enhance the resolution of near-wall turbulence, they observed improvements of turbulence statistics and spectra within the surface layer, but no appreciable difference above, to which they suggested that small-scale features (relative to the LES grid) in the surface layer do not propagate very far upward into the mixed layer. Here, the scales of interest are those associated with organized convection, and their ability to influence and propagate into the mixed layer is investigated. In addition, the dynamic feedback from the mixed layer to the surface layer should also be assessed. It is desirable for the proposed approach if the mixed-layer influence on the surface layer is small, since only the surface-layer grid is refined.

In the following, the coupling between the surface layer and the rest of the CBL is first examined in section 3 through a linear analytic model of the CBL, focusing on the onset of thermal instability. The nonlinear CBL is then simulated in a one-way nested configuration and compared to an LES and a stand-alone gray-zone run in section 4 to further examine the influence of surface-layer convection on the mixed layer in terms of higher-order statistics and convective structures.

## 3. Analytic model of the CBL

The governing equations for the Rayleigh–Bénard thermal instability are adapted to analyze the onset of CBL convection (Piotrowski et al. 2009; C14; ZSC14). With an eddy-diffusion representation of the turbulent fluxes, the normalized Boussinesq equations for CBL convection are given by

$$\frac{\partial u_i^*}{\partial t^*} = -\frac{\partial p^*}{\partial x_i^*} - \mathrm{RaPr}\theta^*\delta_{i3} + \mathrm{Pr}\frac{\partial^2 u_i^*}{\partial x_j^{*2}}, \tag{2}$$

$$\frac{\partial \theta^*}{\partial t^*} - w^* = \frac{\partial^2 \theta^*}{\partial x_i^{*2}}, \quad \text{and} \tag{3}$$

$$\frac{\partial u_i^*}{\partial x_i^*} = 0, \tag{4}$$

where $\mathrm{Ra} = -N^2 z_i^4/(k_t \nu_t)$ is the Raleigh number, $N^2 = g/\theta_0\, d\theta/dz$ is the buoyancy frequency squared, $\mathrm{Pr} = \nu_t/k_t$ is the turbulent Prandtl number, and $\nu_t$ and $k_t$ are the eddy viscosity and diffusivity, respectively. Variables with superscript asterisks are normalized following Drazin and Reid [2004, their Eq. (8.5)]. Derivations of the governing equations are given in ZSC14. To solve the system of equations, the vertical profile of $\Theta$ is required. Piecewise linear approximations, which are sufficient for the purpose of this study, are adopted for $\Theta(z)$ in a classic CBL presented in Fig. 1.

Based on the approximations of $\Theta(z)$, the CBL is simplified into a two-layer structure consisting of an unstable surface layer and a neutral mixed layer. For the mixed layer where $d\Theta/dz = 0$, Eqs. (2) and (3) are further simplified to

$$\frac{\partial u_i^*}{\partial t^*} = -\frac{\partial p^*}{\partial x_i^*} + \mathrm{Pr}\frac{\partial^2 u_i^*}{\partial x_j^{*2}} \quad \text{and} \tag{5}$$

$$\frac{\partial \theta^*}{\partial t^*} = \frac{\partial^2 \theta^*}{\partial x_i^{*2}}. \tag{6}$$

Unlike the surface layer described by Eqs. (2) and (3), $u_i^*$ and $\theta^*$ are decoupled in the mixed layer and no longer depend on Ra. The pure diffusive nature of Eq. (6) suggests that $\theta^*$ is dynamically stable to all initial perturbations. The set of equations for the mixed layer is inherently neutral (stabilitywise) and should only passively respond to forcings from its lower boundary (i.e., the interface between the surface and mixed layers).

Next, we investigate whether the convection patterns in the mixed layer conform to those generated from instabilities at the surface layer. Following the classical analysis procedures of Drazin and Reid (2004), and using normal modes $W(z)f(x, y)e^{st}$ for $w$ and $T(z)f(x, y)e^{st}$ for $\theta$, the governing equations for the surface and the mixed layers are transformed to

$$\text{surface layer:}\quad \overbrace{[D^2(z) - K^2 - s]T(z) = -W(z)}^{\text{Vertical}},$$
$$\overbrace{\nabla_H^2 f(x,y) + K^2(x,y) = 0}^{\text{Horizontal}} \tag{7}$$

$$\text{mixed layer:}\quad [D^2(z) - K^2 - s]T(z) = 0,$$
$$\nabla_H^2 f(x,y) + K^2(x,y) = 0, \tag{8}$$

respectively. Here, $D = d/dz$, $\nabla_H^2 = \partial^2/\partial x^2 + \partial^2/\partial y^2$, and $K = \sqrt{k_x^2 + k_y^2}$ is the horizontal wavenumber. The reduced wave equation $\nabla_H^2 f + K^2 f = 0$ governs the pattern of the horizontal convective structures of the CBL (e.g., hexagonal cells or rolls). Since the reduced wave equation remains unchanged for the surface and mixed layer, the resulting convective structures should also be the same for both layers at the onset of thermal instability.

To further illustrate how the mixed layer responds to the surface layer in the two-layer model, the vertical component of the mixed-layer Eq. (8) is solved directly,

$$T(z) = C_T \exp(-Kz), \qquad W(z) = C_W \exp(-Kz). \tag{9}$$

Both $T(z)$ and $W(z)$ in the mixed layer decay exponentially with height, where $C_T$ and $C_W$ are coefficients determined by the boundary conditions at the interface of the surface and mixed layer.

In the above analysis, the CBL is separated into two layers with linear base-state $\Theta$ profiles and capped by a strongly stable inversion. The governing equations of Rayleigh–Bénard convection apply to the surface layer, predicting convective instability as a function of Ra. In the mixed layer, velocity and potential temperature are decoupled and not dependent on Ra. The prognostic potential temperature [Eq. (6)] is purely diffusive with an exponentially decaying solution given by Eq. (9). The mixed layer responds to forcings from the surface layer below. The convective structures in the surface and mixed layer are governed by the same reduced wave equation [Eqs. (7) and (8)]. Therefore, we expect unchanging convective structures as they initiate in the surface layer and pass through the interface into the mixed layer. Overall, the analytic two-layer model of the CBL suggests that the surface-layer convective instability determines the dynamics of the mixed layer at the onset of resolved convection.

## 4. Nested simulation of the CBL

The linear stability analysis from the analytic model in section 3 is only valid for small-amplitude perturbations and is no longer appropriate when vigorous convection is set in motion. To extend the results from the analytic model and further investigate the nonlinear coupling between the surface layer and the rest of the CBL, an a priori analysis based on one-way nested simulations of the CBL is carried out.

### a. *Numerical setup*

#### 1) CASE DESCRIPTION

The test case is based on the well-studied Australian Wangara experiment (Clarke et al. 1971). It describes a time-evolving CBL from 0900 to 1800 LST for day 33 (16 August 1967) of the experiment. The case setup follows Yamada and Mellor (1975). The atmosphere is initialized with an observational sounding at 0900 LST. A time-varying surface flux boundary condition is applied uniformly to drive daytime heating:

$$\varphi = \sin\left[\frac{\pi}{11}(t + 1.5)\right],$$
$$\overline{w'\theta'}_s = 0.216\,(\mathrm{K\,m\,s^{-1}})\varphi, \tag{10}$$

where $t(h)$ is set to 0 at the beginning of the simulation and $Q_s$ ($\mathrm{K\,m\,s^{-1}}$) is the surface sensible heat flux. Temporally constant geostrophic winds $U_g$, $V_g$ ($\mathrm{m\,s^{-1}}$) are applied to represent synoptic pressure gradients,

$$U_g = \begin{cases} 0.0029\,(\mathrm{s^{-1}})z - 5.5\,(\mathrm{m\,s^{-1}}) & 0 \le z < 1000 \\ 0.0014\,(\mathrm{s^{-1}})z - 4\,(\mathrm{m\,s^{-1}}) & z \ge 1000 \end{cases}, \quad V_g = 0. \tag{11}$$

Simulations are performed on a doubly periodic domain of size 38 km × 38 km × 2.5 km. Uniform vertical grid spacing of 50 m is adopted. Rayleigh damping is applied to the top 500 m of the domain.

The Advanced Regional Prediction System (ARPS) is used for the simulations. ARPS is a nonhydrostatic mesoscale and convective-scale finite-difference numerical weather prediction model. It uses a generalized height-based terrain-following coordinate on an Arakawa C grid. A mode-splitting time integration scheme is employed with vertically implicit treatment for sound waves (Klemp and Wilhelmson 1978). More details about ARPS, including its SGS and PBL mixing schemes, are documented in Xue et al. (2000, 2001).

### 2) Numerical algorithms

A list of key model parameters is presented in Table 1. The first simulation (50L) is an LES with 50-m isotropic grid spacing, using Deardorff (1974)'s 1.5-order TKE scheme as turbulence closure. Results from the 50L run are processed and saved at every time step, as explained in the following paragraphs. In addition, 50L also serves as a high-resolution benchmark of the Wangara CBL.[3] The second simulation (950G) has a uniform horizontal spacing of 950 m. Following Xue et al. (1996), the ARPS PBL scheme based on Sun and Chang (1986) is used for vertical mixing.

The third simulation (950G-50L) is a reverse one-nested run designed to test the response of the mixed layer and above to surface-layer forcings. Its domain is identical to 950G, while a fine nest grid of 50-m spacing occupies the bottom five levels of the parent grid. The reverse nesting procedure starts with the 50L run. At every time step of the 950G-50L run, results from 50L are mapped to the 950-m grid through flat spatial averaging:

$$\Phi_{IJ} = \frac{1}{R_x}\frac{1}{R_y}\sum_i\sum_j \phi_{ij}, \qquad (12)$$

where $\Phi_{IJ}$ and $\phi_{ij}$ represent the prognostic variables including velocity, potential temperature, and pressure; and $R_{x,y} = \Delta_{x,y}/\delta_{x,y}$ are the nesting ratios in the $x$ and $y$ directions. In this case, $R_x = R_y = 19$; $(I, J)$ and $(i, j)$ are indices of overlapping grid points on the parent and nest grid. The summations are operated over the stencil $[i-(R_x-1)/2, i+(R_x-1)/2]$ and $[j-(R_y-1)/2, j+(R_y-1)/2]$. The general procedure of filtering (averaging) fine-grid data to the coarse grid is termed "anterpolation" by Sullivan et al. (1996). The choice of the averaging operator follows that of Clarke et al. (1971) to satisfy the conservation (or reversibility) condition. Special care is taken when downscaling higher-order tensors from the fine grid (Sullivan et al. 1996). Since the Sun and Chang (1986) PBL scheme is based on a prognostic TKE equation, TKE from the

[3] ZSC14 showed that the Wangara CBL is well resolved at 50-m isotropic spacing, where higher-order statistics and spectra have converged.

TABLE 1. List of model parameters; $\Delta_{x,y}(\delta_{x,y})$ is the horizontal grid spacing for the parent (nest) grid; $N_{x,y}(n_{x,y})$ is the number of horizontal grid points on the parent (nest) grid; $n_z$ is number of vertical grid points for a nested run; $\Delta t$ is the large time step of the simulation. Runs are named with their respective horizontal grid spacing. The letters L (for local) and G (for global) are appended at the end of the run names to distinguish runs with the LES and the PBL schemes for turbulent mixing. Parent and nest variables are distinguished by capital and small letters. The 950G-50L is the control nested run, which is also named N6 for comparison purposes in the sensitivity study. The 950G-50L-D uses a dynamic nest level that is based on 15% of $\langle z_i(t)\rangle$ and increases from 2 to 6 for the Wangara CBL.

| Type | Name | $\Delta_{x,y}(\delta_{x,y})$ (m) | $N_{x,y}(n_{x,y})$ | $n_z$ | $\Delta t$ (s) |
|---|---|---|---|---|---|
| Stand-alone | 50L | 50 | 760 | — | 0.5 |
| Stand-alone | 950G | 950 | 40 | — | 4 |
| Nest | 950G-50L/N6 | 950 (50) | 40 (760) | 6 | 4 |
| Nest | N16 | 950 (50) | 40 (760) | 16 | 4 |
| Nest | N26 | 950 (50) | 40 (760) | 26 | 4 |
| Nest | 950G-50L-D | 950 (50) | 40 (760) | 2–6 | 4 |

50-m LES run is also mapped to the 950-m grid. In addition to averaging the SGS components, additional TKE, which is resolved on the 50-m grid, but of subgrid scale on the 950-m grid, is also accounted for

$$E_{IJ} = \frac{1}{R_x}\frac{1}{R_y}\sum_i\sum_j e_{ij} + \frac{1}{2}\left\{\left[\frac{1}{R_x}\frac{1}{R_y}\sum_i\sum_j (u_{ij}^2 + v_{ij}^2 + w_{ij}^2)\right] - (U_{IJ}^2 + V_{IJ}^2 + W_{IJ}^2)\right\}. \qquad (13)$$

Finally, the bottom 10 vertical layers of the spatially averaged variables are saved at every time step of the 950G-50L run.

Next, 950G-50L is performed on a 950-m horizontally spaced grid. After every time step, all prognostic variables ($u$, $v$, $w$, $\theta$, $p$, and $e$) in the bottom six vertical model levels are replaced by the averaged (filtered) 50L data. Since vertical level 1 is a ghost level below the surface, the heights of $u$, $v$, and $w$ points at level 6 are 225 and 200 m, respectively. Vertical layers from levels 7 to 10 are set as a buffer zone for a smooth transition from the bottom 6 anterpolated layers to the coarse grid above. Prognostic variables in the buffer zone are a linear combination of the anterpolated 50L (denoted by superscript $a$) and the original 950G-50L results:

$$\Phi_{IJK} = \begin{cases} \Phi_{IJK}^a & K < 7 \\ \dfrac{11-K}{5}\Phi_{IJK}^a + \dfrac{K-6}{5}\Phi_{IJK} & 7 \le K \le 10 \end{cases}. \qquad (14)$$

The above procedures constitute a reverse one-way nest, where the fine-grid simulation is performed prior to the nest simulation. Data from the fine-grid run are filtered and fed into the nest coarse-grid run. The purpose of this run is to investigate how the mixed layer responds to surface-layer forcings in a 3D simulation. Relating to the proposed gray-zone approach, it also serves to investigate the potential improvements of the overall CBL simulation by explicitly resolving the surface layer only. For these reasons, the quality of the numerically simulated surface layer must be ensured. Therefore, data from the nest domain are postprocessed from an independent 50-m LES, where the surface layer is well resolved.

The choice of 950-m spacing for the parent grid is based on the practical considerations of the proposed approach. The grid-refinement-based approach requires fine grid spacings to resolve the surface layer reasonably well. For a ~1-km-deep CBL, the surface-layer grid spacings must be no coarser than ~400 m (Xue et al. 1996). On the other hand, a refinement ratio of 3 or 5 is typical for grid nesting (Warner et al. 1997). Larger ratios can cause a long transition fetch in the fine nest where smaller resolvable scales are successively generated (Muñoz-Esparza et al. 2014). Given an approximate upper limit for the fine nest grid spacing of 400 m and a 5:1 refinement ratio, the parent grid spacing should not exceed 2 km in practice. We did perform another set of simulations at 1950-m grid spacing including a stand-alone gray-zone run and two nested simulations with 6 and 16 vertical nest levels. The results are qualitatively similar to that from the 950-m grid spacings and therefore not presented.

For the method to work with 4-km grid spacing, which is the approximate upper limit of the CBL gray-zone range (Honnert et al. 2011), a larger nest ratio is required. This can be achieved if numerical methods are implemented to minimize the transition fetch. For example, a nest ratio of 11 is used by Muñoz-Esparza et al. (2017) for a real-case simulation by perturbing the inflow to accelerate the generation of small-scale turbulence on the nest grid. In the current nest setting, the transition fetch is irrelevant because the fine nest is run independently. A refinement ratio of 19 is used deliberately to feed a well-resolved surface layer into the parent gray-zone grid.

The choice of the bottom six layers for the vertical nest is made because the surface layer usually occupies 10%–15% of the CBL. For the Wangara case, where the daytime CBL depth reaches its peak of 1.5 km in the late afternoon, the surface-layer depth is roughly 200 m at its maximum. During the course of the day, the surface-layer depth deepens in proportion to a deepening $z_i$ (as shown later in Fig. 4). Strictly, if only the surface is to be refined, the nest-layer depth should vary with $z_i$, while the relative surface-layer to boundary layer depth ratio is kept fixed. This is implemented in an additional simulation whereby the depth of the nested layer is kept at the bottom 15% of the horizontally averaged CBL depth at every time step. Selected results of the dynamic nest-level run are presented in section 4b. Overall, simulation results from the dynamic nest level are very similar to that from the static nest level. While implementing a dynamic nest level is simple for the one-way nested configuration presented in this study, it gets complicated considerably for two-way nesting in a separate paper. Therefore, we kept using static levels for both the one-way and two-way nested simulations. In the gray-zone parameterization of C14, the unstable-layer depth is also set to a fixed 300-m depth for a 1-km-deep CBL, which is twice as deep as the current setting. Two more simulations are performed where the nest occupies the bottom 16 and 26 layers (the N16 and N26 simulations, respectively). Together with the six-layer control run (N6), results from these three nest simulations investigate the model sensitivity toward the depth of the grid-refinement zone.

### b. Results and discussion

#### 1) FIRST-ORDER STATISTICS

Figure 3 compares the vertical profiles of potential temperature $\langle\Theta\rangle$ among the stand-alone 50L and 950G runs and the nested 950G-50L run with six nest layers. Here, the angle brackets represent horizontal averaging. Overall agreement is achieved for the three runs. As explained in ZSC14, as long as turbulent mixing is sufficient, all first-order statistics should exhibit well-mixed profiles, regardless of the nature of the mixing mechanisms in the model. In the 50L run, turbulent mixing is mostly carried out by explicitly resolved convective motions plus a small fraction of SGS mixing through the turbulence closure. In 950G, SGS mixing by the PBL scheme is primarily responsible for most of the turbulent mixing, and hardly any resolved motions exist in the first few hours of the simulation. Below 225 m, profiles of $\langle\Theta\rangle$ from the nested simulation are identical to that from 50L. This is expected because the bottom six levels of 950G-50L are obtained by averaging the 50L data. In the buffer zone between 225 and 425 m, the profiles of the nested run gradually deviate from 50L. Initially, at 1200 LST, $\langle\Theta\rangle$ of the nested run nearly overlaps that of 950G above 400 m. Later in the afternoon in Fig. 3, the $\langle\Theta\rangle$ profile of the nested run gradually converges to that of 50L in the upper half of the CBL toward the capping inversion.

The boundary layer depth is shallower in 50L and 950G-50L than 950G. This is confirmed by plotting the

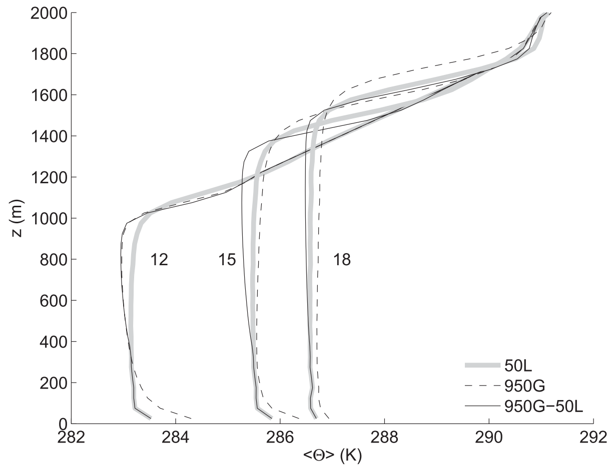


FIG. 3. Comparison of horizontally averaged potential temperature $\langle\Theta\rangle$ at 1200, 1500, and 1800 LST.

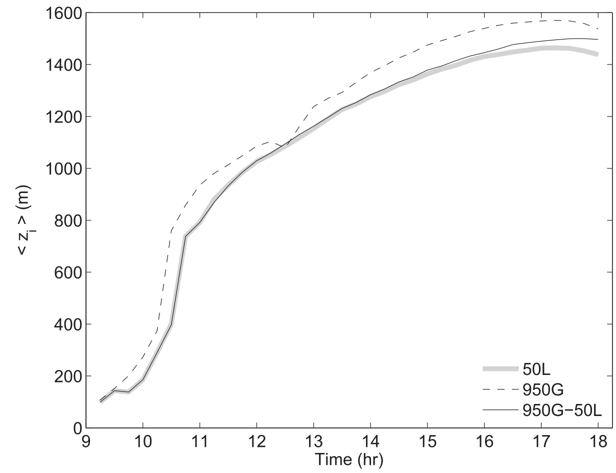


FIG. 4. Time series of horizontally averaged boundary layer depth $\langle z_i\rangle$.

evolution of the boundary layer depth $\langle z_i\rangle$ in Fig. 4. Here, $z_i$ is determined by the elevated level of neutral buoyancy for a surface parcel, the same method as that used in the Sun and Chang (1986) PBL scheme within ARPS. In Fig. 4, $\langle z_i\rangle$ increases with time and reaches its maximum value between 1700 and 1800 LST. The time series of $\langle z_i\rangle$ for 50L and 950G-50L nearly overlap, while 950G predicts a deeper PBL. This is because the PBL-scheme-predicted SGS turbulent mixing is less than sufficient near the surface (Xue et al. 1996). A slightly deeper superadiabatic surface-layer results (see Fig. 3) in order to maintain upward SGS heat flux in the gradient diffusion-based PBL scheme. Because of this, the surface temperature is warmer in 950G, leading to a higher diagnosed $z_i$, therefore, more turbulent entrainment (through SGS mixing) at the CBL top, and finally, a deeper CBL. Since the surface layer of the nested run is averaged from the high-resolution LES run, turbulent fluxes are mostly resolved and better predicted. The improved representation of the surface layer, specifically the depth and shape of the superadiabatic profile, leads to improved diagnoses of the boundary layer depth and subsequently the overall evolution of the CBL.

Notice that in Fig. 3, the $\langle\Theta\rangle$ profile of the nested run is unstable above the buffer zone at 1500 LST. At 1800 LST, it also appears slightly unstable compared with the LES run, although to a lesser extent. Such unstable profiles are likely due to underprediction of entrainment processes in the nested run. To investigate the cause, the entrainment flux ratio $R_H$ is presented in Fig. 5a, where $R_H$ is defined as the ratio of entrainment flux to the surface flux of heat (Holtslag and Moeng 1991). Here, heat fluxes include both resolved and SGS contributions. Note that the surface heat flux is fixed for all runs as boundary conditions [see Eq. (10)]. The $R_H$ from the LES benchmark increases with time, with a value slightly less than 0.2 for most of the day. Such values are within expected ranges of CBL entrainment (Gentine et al. 2015). For the stand-alone gray-zone run, $R_H$ is initially smaller than the benchmark until past 1200 LST when $R_H$ spikes over the LES curve. Such underprediction of entrainment flux on gray-zone grids at the morning transition is also noted in Efstathiou et al. (2016). The spike corresponds to the onset of spurious resolved convection that also leads to the sudden drop of $z_i$ in Fig. 4, as the warm surface air is suddenly mixed upward. (More details on this will be shown later in Fig. 8). Afterward, $R_H$ for 950G increases with time as in 50L, however, with a smaller magnitude. In comparison, the overall pattern of the time series of $R_H$ from 950G-50L is more consistent with that of 50L. The magnitude of $R_H$ is underpredicted throughout the simulation. However, at the beginning, $R_H$ from the nested run is larger than the stand-alone run. This is again related to the improved prediction of the onset of resolved convection in the nested run (as shown later in Fig. 8). Specifically, in 950G-50L, resolved convective plumes contribute to entrainment processes early on in the simulation. When the nest level is raised to 16, the $R_H$ curve initially overlaps that of the six-level run when the boundary layer is still shallow (see Fig. 4). After 1130 LST, $R_H$ from N16 becomes larger than that from N6, although its magnitude is still smaller than that of 50L.

The ratio of resolved to total heat flux is presented in Fig. 5b. First, notice that in 950G before 1130 LST, the resolved entrainment is close to zero, suggesting that the PBL scheme is solely responsible for mixing. When spurious convection sets in, about 60% of the entrainment flux is from the resolved component. This is in

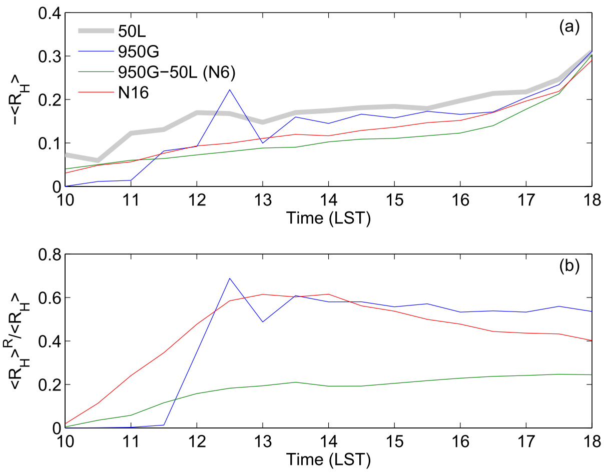


FIG. 5. Time series of (a) the horizontally averaged entrainment flux ratio $R_H$ and (b) the resolved to the total entrainment flux ratio.

violation of the underlying SGS homogeneity assumptions of the PBL scheme. For the nested run 950G-50L, the resolved component is small yet nonzero. Its percentage contribution approaches a little over 20% in the late afternoon. When the nest level is increased to 16, the contribution from the resolved entrainment flux increases significantly to about 50%. But even so, the total entrainment flux is still underpredicted according to Fig. 5a.

Inspection of Fig. 5 indicates that the slightly unstable profile of $\Theta$ above the nest domain in 950G-50L is mostly likely a result of the underprediction of entrainment fluxes. The cause for such underprediction of the total entrainment flux can be traced back to the resolved and SGS components. The resolved to total flux ratio in Fig. 5b reveals that in the entrainment zone of 950G-50L, the PBL scheme is still largely responsible for the vertical mixing. However, as discussed previously, a shallower boundary layer in the nested run due to a better-mixed surface layer (see Fig. 4) leads to a smaller turbulent mixing coefficient, hence less turbulent entrainment of free-tropospheric air with warmer potential temperature. The improvement of surface-layer profiles leading to reduced entrainment fluxes is an unexpected consequence rooted in the design of the PBL scheme. The LES run does not suffer from such effects although its simulated boundary layer depth is similar to that of the nested run, mainly because entrainment is mostly resolved rather than parameterized. At 1800 LST, the unstable $\Theta$ profile almost disappears, because at that time, the entrainment flux ratio of the nested run is closer to the LES and the stand-alone gray-zone runs.

On the other hand, the resolved component of the entrainment flux is also underpredicted in 950G-50L, as evidenced by comparison with the 16-level nested run in Fig. 5b. This is likely due to the presence of stronger thermals when the nest level is raised (as shown later in Fig. 12). As presented in Hunt et al. (1988), CBL thermals gain strength by merging smaller plumes as they rise. The increased nest level helps to nurture stronger thermals as they ascend through the surface and the lower mixed layer. The stronger thermals are able to increase resolved entrainment fluxes as they encroach the capping inversion. Overall, the artifact of a slightly unstable $\Theta$ profile is largely mediated when the nest level is raised (as shown later in Fig. 11).

### 2) HIGHER-ORDER STATISTICS

Vertical profiles of some resolved second- and third-order statistics at 1500 LST are presented in Fig. 6. The time 1500 LST is chosen here and afterward to present results because by then, the CBL is well developed in all runs. In addition, analysis around this time reflects some deficiencies of the analytic model predictions. Alongside results from the first three runs, a fourth run named filtered-50L is presented. It is obtained by applying a spectral filter to 50L at the gray-zone spacing (i.e., 950 m) to represent the ''true'' resolved flow statistics on the gray-zone grid. A 2D Fourier transform is applied to the 50L data at each vertical level. A sharp low-pass spectral filter is applied where amplitudes of horizontal wavelengths smaller than $2 \times 950$ m (i.e., the Nyquist grid cutoff) are zeroed. The data are then inverse-Fourier-transformed to physical space where statistics are computed. Here, 2D horizontal filtering is used to approximate 3D filtering. This is justified in Tong et al. (1998) and has also been used in Sullivan and Patton (2011).

In comparing profiles from the ideal (filtered-50L) and the actual (950G) gray-zone runs, potential problems of gray-zone modeling using conventional PBL schemes are exposed. In terms of resolved variances, although general agreement is achieved for $\langle\overline{w'w'}\rangle$, the profiles of $\langle\overline{u'u'}\rangle$ are very different between the filtered-50L and the 950G runs. The $\langle\overline{u'u'}\rangle$ in 950G not only exceeds the true solution at all elevations, it also exceeds the original 50L run below $z/z_i \sim 0.3$ and above $z/z_i \sim 0.6$. The agreement in the vertical and disagreement in the horizontal velocity variances are explained by ZSC14, because $\langle\overline{w'w'}\rangle$ is a function of the vertical structure of the CBL only, while $\langle\overline{u'u'}\rangle$ also depends on the horizontal wavenumbers. In comparison, $\langle\overline{u'u'}\rangle$ in the nested run agrees well with the filtered LES solution, although it is slightly smaller toward the CBL top.

The $\langle\overline{w'w'}\rangle$ profile in the nested run deviates from the filtered LES solution above $z/z_i \sim$ 0.2 and is also smaller than the 950G solution. Such underprediction is most

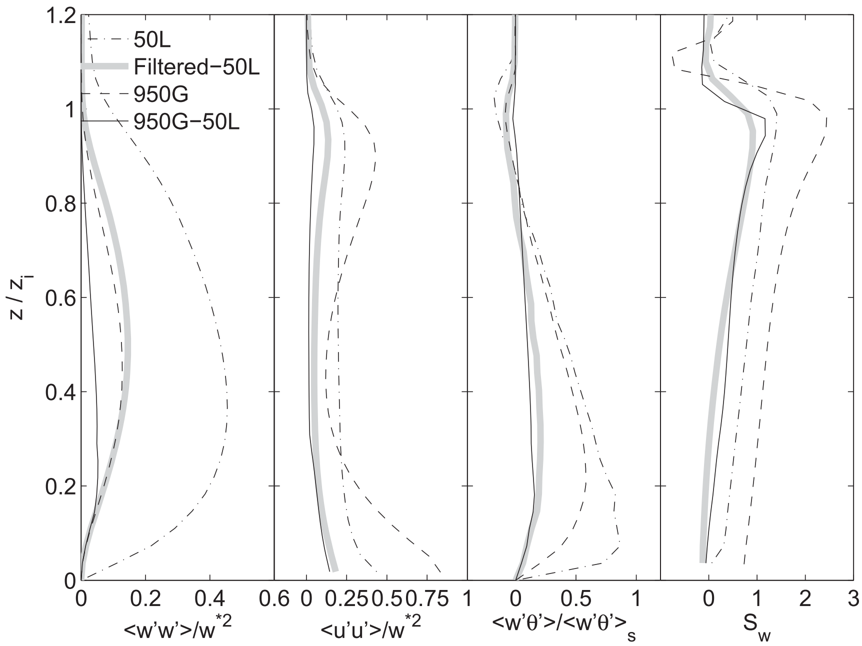


FIG. 6. Horizontally averaged (from left to right) resolved $w$ variance, resolved $u$ variance, resolved sensible heat flux, and skewness of the vertical velocity at 1500 LST. Variances are normalized by $w^{*2}$, where $w^* = [(g/\Theta_0)\overline{w'\theta'}_s z_i]^{1/3}$ is the free-convective velocity. Sensible heat flux is normalized by its surface value $\overline{w'\theta'}_s$.

likely a result of the lack of feedback from the mixed layer in the parent grid to the surface layer in the nest grid. In the current one-way nest model, flow in the surface layer is obtained by the averaged LES data at every time step. Two-way coupling between the surface and the mixed layer is reduced to a one-way interaction, since flow in the surface layer is not affected by the mixed layer according to the ''reverse nest'' procedure. Under such a setting, the analytic model predicts that the prognostic momentum and potential temperature equations are decoupled in the mixed layer [see Eqs. (5) and (6)]. Under the Rayleigh–Bénard framework, $\langle w'w' \rangle$ scales with $W(z)^2$ [ZSC14, their Eq. (15)] and therefore should decay exponentially upward above the surface layer according to Eq. (9). In comparison, $\langle u'u' \rangle$ as function of the horizontal wavenumber [ZSC14, their Eq. (15)] is less affected. This is because the horizontal convective structures in the mixed layer do conform to those generated in the surface layer (shown later in Fig. 10). Comparison between the nest and the filtered LES run reveals the feedback from the mixed layer to the surface layer, which is not captured by the analytic model. When the surface and the mixed layers are allowed to interact in a two-way nested simulation in a separate paper, the underprediction of $\langle w'w' \rangle$ is indeed reduced.

The resolved heat flux $\langle \overline{w'\theta'} \rangle$ of the 950G run is larger than that of the filtered LES run. This suggests a biased partition of $\langle \overline{w'\theta'} \rangle$ between the resolved and SGS components. Part of $\langle \overline{w'\theta'} \rangle$ that should have been carried by smaller (SGS) eddies on the 950-m grid are erroneously cast into the large (resolved scale) eddies. (This will become clearer in the velocity spectra presented in Fig. 10.) In comparison, the resolved $\langle \overline{w'\theta'} \rangle$ in the nested run agrees well with the filtered LES. The negative (entrainment) flux at the top of the CBL in the nested run is less than that in the filtered-50L and the 950G runs. This is likely a result of the underpredicted mixing coefficient near the CBL top as explained in section 4b(1), since turbulent mixing in the coarse grid above the nest surface layer is still predicted by the PBL scheme.

The skewness of the vertical velocity $S_w$ of the 950G run is larger than that of the filtered-50L run as well as the original 50L run throughout the depth of the CBL. In comparison, $S_w$ of the nested run nearly overlaps that of the filtered LES. The large differences in $S_w$ suggest overall different probability density distributions of the vertical velocity, which are approximated by discrete histograms in Fig. 7 at two elevations. The histograms are normalized such that the area under each curve is unity. In both the surface layer ($z/z_i = 0.1$) and center of the CBL ($z/z_i = 0.5$), the histograms are strongly positively skewed for 950G, whereas both the filtered LES and the nested results exhibit slight positive skewness. In the surface layer, the nested and the filtered LES

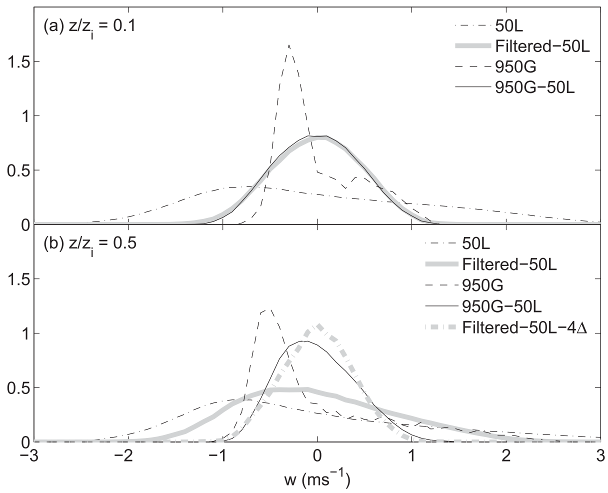


FIG. 7. Normalized histogram of the vertical velocity at $z/z_i$ = (a) 0.1 and (b) 0.5 at 1500 LST. Bin size is 0.1 m s$^{-1}$.

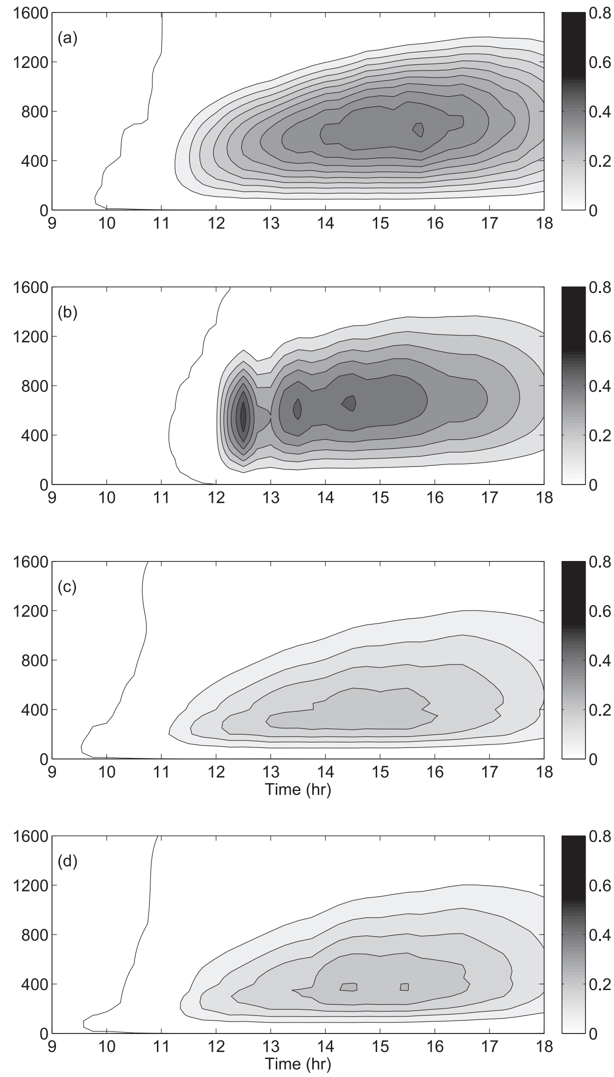


FIG. 8. Time–height contours of $\langle w'w' \rangle$ from (a) filtered-50L, (b) 950G, (c) 950G-50L, and (d) 950G-50L-D. Contour interval is 0.05 m$^2$ s$^{-2}$. The leftmost contour is at $1 \times 10^{-4}$ m$^2$ s$^{-2}$.

histograms overlap because the nested run at that level is obtained from spatial averaging (filtering) the LES run. Higher up, the range of $w'$ for the nested run is narrower than the filtered LES run, although their skewness is almost the same (see Fig. 6). This is because for atmospheric models such as ARPS and WRF, the effective grid resolution is usually coarser than the Nyquist cutoff, because of both the numerical discretization and the explicit or implicit computational mixing applied for damping poorly resolved waves. The histogram of $w'$ at $z/z_i = 0.5$ of the nested run does compare better with filtered LES at $4 \times 950$ m in Fig. 7b.

The onset of resolved convection for the three simulations is presented in Fig. 8 to check the validity of the conclusions from the analytic model. The onset timing for each run at each elevation is determined by the instance when the resolved $\langle \overline{w'w'} \rangle$ first exceeds a threshold value, set to $1 \times 10^{-4}$ m$^2$ s$^{-2}$. It is a small arbitrary number that corresponds to $w' \sim 0.01$ m s$^{-1}$. Higher thresholds translate the curves to the right at all elevations and do not affect the comparison between the three runs. The use of resolved variances of other prognostic variables results in qualitatively similar curves. In Fig. 8a, the onset of convection for the filtered 50L is shortly after the beginning of the simulation at 0900 LST. The positive gradient of the leftmost contour suggests that the resolved convection is found at later times at higher elevations, in accordance with the surface-initiated instability. The onset of resolved convection for the stand-alone gray-zone run is delayed by more than an hour in Fig. 8b. The reason for the delay in the onset of convection is the grid-based critical Ra on the gray-zone grid as explained in ZSC14. Between 1200 and 1300 LST when resolved convection is initiated on the gray-zone grid, a pulse release of $\langle w'w' \rangle$ of large magnitudes is found in 950G. In comparison, the onset of resolved convection for 950G-50L is much closer to the filtered LES results. The magnitude of the $\langle w'w' \rangle$ in the nested run is however smaller than the filtered LES run.

Figure 8d presents $\langle w'w' \rangle$ for the dynamic nest-level run 950G-50L-D. In theory, the static nest-level run 950G-50L should be better than the dynamic nest-level run. This is because in the early morning, a larger proportion of the CBL is resolved with 950G-50L. As the surface layer deepens in proportion to $z_i$ toward later afternoon, the dynamic nest level increases to the static nest level. However, no appreciable differences are found in the results of the static (Fig. 8c) and dynamic

(Fig. 8d) nest-level runs. Other first- and second-order statistics are also very similar between the two simulations (results not shown). This reinforces the conclusion of this study; that is, if the grid spacing of the surface layer is refined to explicitly resolve convection where it originates, the overall simulation of the CBL is expected to improve.

#### 3) Flow visualization and spectral comparison

The probability density distributions, along with its first (mean) and higher-order moments (variance and skewness) reveal large differences between the ideal and the actual gray-zone runs. Compared to the stand-alone gray-zone run, the nested run exhibits improvements above the surface layer for the overall CBL in general except for the resolved vertical velocity variance. Apart from statistical properties, visualizations of instantaneous flow fields at 1500 LST in Fig. 9 offer a direct comparison of the simulated convection for three different runs and the filtered LES run. In the LES run, organized cell patterns stand out in the $w'$ field (see Fig. 9a), where red colors represent narrow updrafts and blue colors represent broad compensating subsidence. At higher elevations (see Fig. 9b), cells broaden because of merging of small plumes (Hunt et al. 1988). For 950G (Figs. 9g and 9h), organized structures that are qualitatively similar to those found in Figs. 9a and 9b are evident but are much broader. In the filtered-50L run (Figs. 9c and 9d), organized convective structures are much less pronounced. This is because the lengths of the cells (i.e., the dominant length scale of the CBL) in Figs. 9a and 9b are around the boundary layer depth. Filtering at 950 m removes a large portion of the energetic eddies, as evidenced in the reduced resolved variances in the filtered-50L compared to the 50L run in Fig. 6. The nest flow field is nearly identical to the filtered-50L field at $z/z_i = 0.1$ as a result of the nesting procedure. It is also close to the filtered LES outside the nest region at $z/z_i = 0.5$, although the magnitude is somewhat reduced. The comparison improves when the LES flow field is filtered to 4 instead of $2 \times 950$ m (results not shown).

To quantitatively assess the dominant length scales in different runs, the energy spectra as a function of the horizontal wavelength $\lambda = 2\pi/\sqrt{k_x^2 + k_y^2}$ are plotted in Fig. 10. The spectral peak is a good estimate of the length scale of the dominant eddies (Kaimal and Finnigan 1994). The spectral peaks of 950G are at a much larger wavelength than that of 50L in all subplots of Fig. 10. The magnitude of the spectral peaks in the $u$ spectra for 950G even exceeds that of 50L in Figs. 10b and 10d. In comparison, the spectra of the nested run almost overlap those of 50L toward the long-wavelength end, since eddies of that size are well resolved on both the 50- and 950-m grid. At $z/z_i = 0.1$ (Figs. 10a and 10b), spectral magnitudes of the nested run decrease toward small wavelengths as a result of the flat averaging operator in physical space. At $z/z_i = 0.5$ above the nest region (Figs. 10c and 10d), the spectral magnitude also decreases toward small wavenumbers because of the poorly resolved high wavenumber modes and computational mixing. At the wavelength cutoff of $2 \times 950$ m, the nested spectra are zero because of the resolution limit. Overall, the spectra of the nested run are much better behaved than the stand-alone run. The nested run does not create spurious spectral peaks and conforms to the 50L run for long resolvable wavelength.

#### 4) Sensitivity to nest layers

To test model sensitivity to the depth of the grid-refinement layer, two additional runs are performed. These runs are nested up to 725 and 1225 m, which are roughly half the CBL depth, and up to the entrainment zone at 1500 LST. The horizontally averaged $\Theta$ profiles are presented in Fig. 11. Deeper nest layers show improvements over the control nested run. Profiles of the N16 run are very close to those of the 50-m LES run except for small differences in the entrainment zone around 1500 LST. The profiles from the N26 and the 50L runs almost overlap completely. The slight superadiabatic gradient in the upper half of the CBL in the control run N6 is already removed in N16, let alone N26. The profiles remain neutral in the upper half of the CBL, outside the nested region in N16.

Improvements are also found in higher-order statistics as presented in Fig. 12. Profiles of the 50L and 950G runs are removed for clarity. For all statistics, N26 is close to filtered-50L as a result of the elevated refinement level almost up to $z/z_i \sim 1$. The differences primarily result from flat and spectral averaging. The former is not spectrally sharp, hence affects low wavenumbers beyond the filter width. Successive improvements toward the filtered LES run are found as the depth of the nest layer increases, especially for the $\langle w'w' \rangle$ profiles. With grid refinement up to half the CBL depth, the N16 profiles already exhibit overall agreement with the filtered-50L run. Note that for skewness $S_w$, the overprediction toward the CBL top is a result of flat averaging. Around the CBL top, skewness is large as a result of the overshooting thermals. When flat averaging is applied there, it tends to overeliminate the downward motions, hence increase skewness.

## 5. Summary

PBL schemes are inappropriate at gray-zone resolutions because of the violation of their underlying

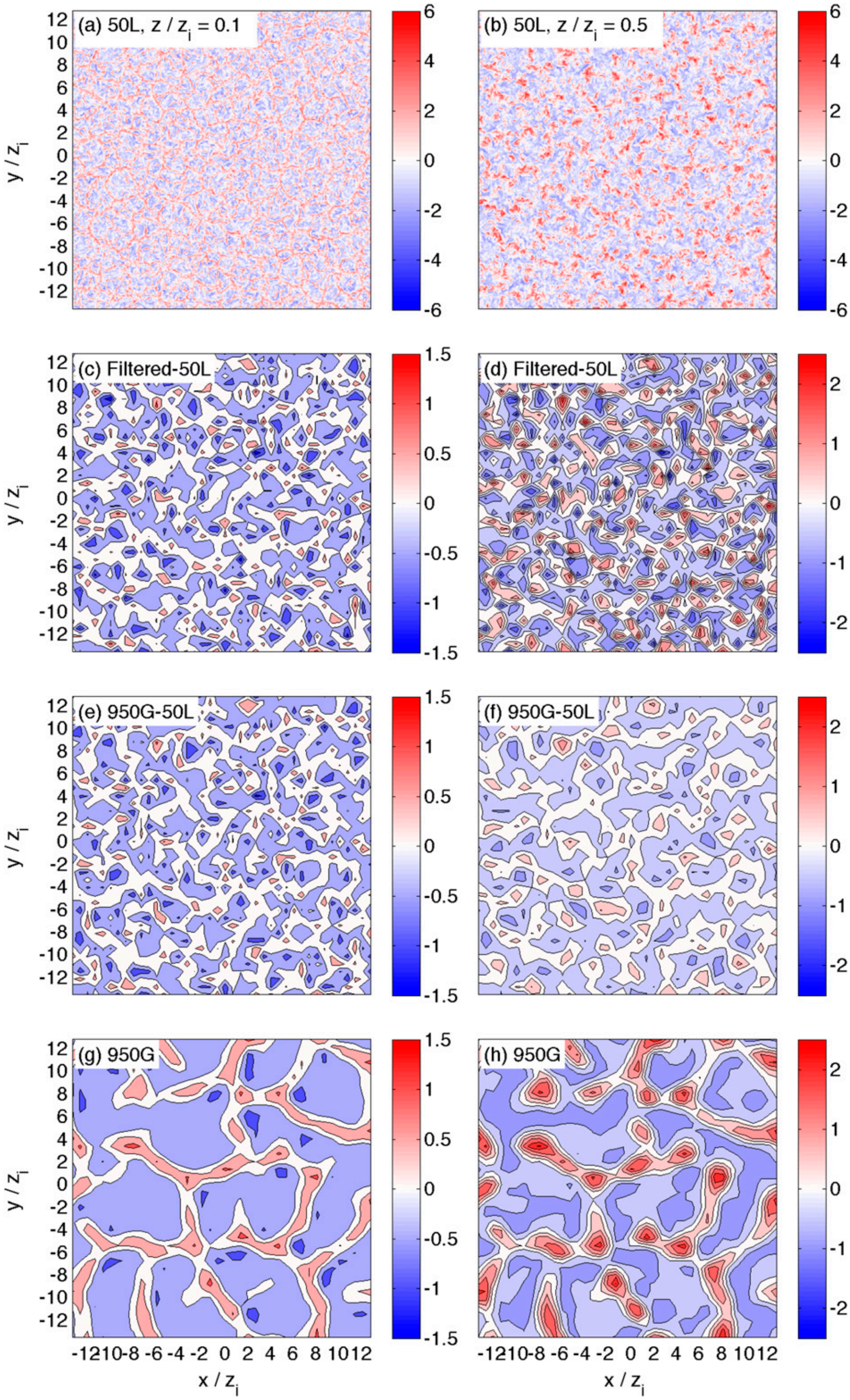


FIG. 9. Visualization of $w'$ from (a),(b) 50L. Horizontal contours of $w'$ from (c),(d) the filtered 50L, (e),(f) 950G-50L, and (g),(h) 950G runs at (left) $z/z_i = 0.1$ and (right) $z/z_i = 0.5$ at 1500 LST. Contour interval is $0.5\ \mathrm{m\,s^{-1}}$.

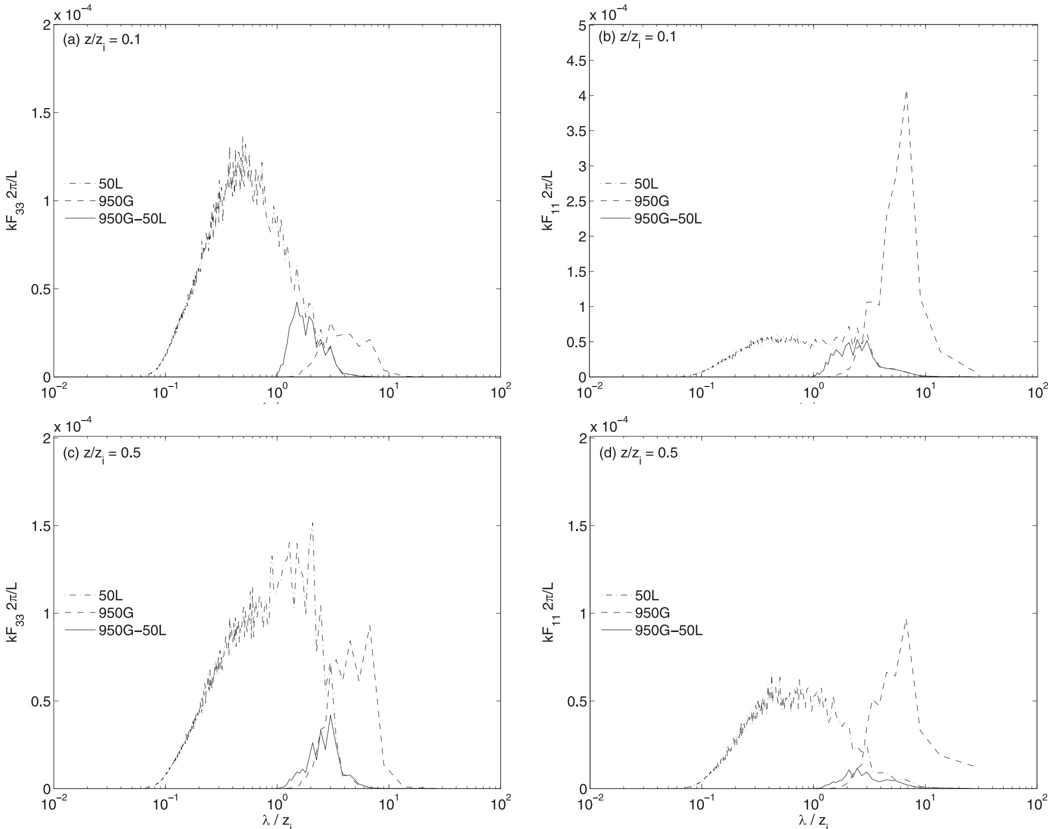


FIG. 10. The (a),(c) $w'$ and (b),(d) $u'$ energy spectra at (left) $z/z_i = 0.1$ and (right) $z/z_i = 0.5$ from the 50L, 950G, and 950G-50L runs at 1500 LST. Note that the $y$ axis in (b) is different from the rest.

horizontal-homogeneity assumption on the subgrid scale. Such violation leads to delayed onset of resolved convection and spurious convective structures (C14; ZSC14). Targeting such deficiencies of PBL schemes on the gray-zone grids, several studies have proposed scale-aware PBL schemes by using empirically determined flux-partition functions to downweight the SGS flux of the original PBL schemes (Boutle et al. 2014; Shin and Hong 2015; Efstathiou et al. 2016). Alternatively, C14 designed an approach based on the dynamical role of the surface layer in controlling resolved CBL convection. They showed that when spurious resolved convection in the surface layer is suppressed by increased horizontal diffusion, it also disappears in the mixed layer. Inspired by C14's approach, we raise the following question. On a gray-zone grid, if the most energetic scales of convection are properly resolved in the surface layer, will they also be properly resolved in the mixed layer? If so, a grid-refinement-based approach can be designed to explicitly resolve the most energetic scales of surface-layer convection and, in turn, to improve the overall CBL simulation. When spurious surface-layer convection is controlled by either elimination as done in C14 or explicit resolution proposed in this study, deficiencies of the PBL schemes on the gray-zone grid can be ameliorated.

To conceptually justify the proposed approach, we must show that if convection is properly resolved in the surface layer, it is also properly resolved in the mixed layer despite the gray-zone grids. To do so, we must study the dynamic coupling between the surface layer and the rest of the CBL. Based on an analytic model and one-way nested simulations, it is shown that convection from the surface layer largely determines the dynamics of the mixed layer and above. This provides the theoretical basis for the grid-refinement-based approach for modeling the CBL at gray-zone resolutions. The main conclusions from the analytic model and the nested 3D simulations are summarized below.

First, a two-layer analytic model is constructed for the CBL to focus on the onset of thermal instability. The surface-layer dynamics are governed by the classical Rayleigh–Bénard equations. In the neutrally stratified mixed layer, momentum and temperature equations are decoupled. The vertical structures in the mixed layer are

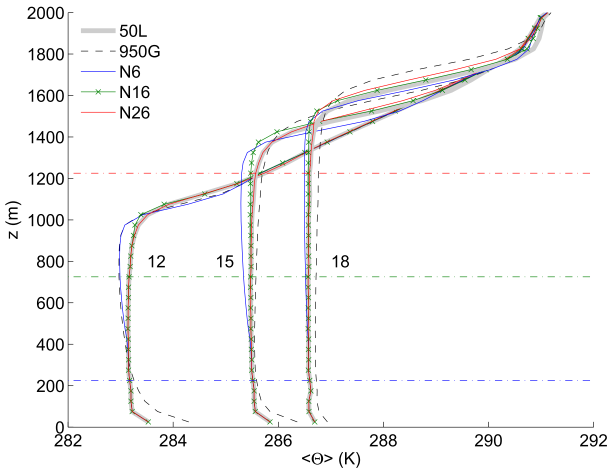


FIG. 11. As in Fig. 3, but for two additional runs with higher nest levels. The three horizontal dashed lines correspond to the height of the nest grid at 225, 725, and 1225 m. Note that the 950G-50L run is renamed N6 for ease of comparison.

therefore set by the boundary conditions at the interface between the surface and the mixed layer and decay exponentially upward. The reduced wave equations that govern the horizontal motions are the same in the surface and the mixed layers, suggesting consistent horizontal convective structures in both layers. In the two-layer model, the surface layer assumes a dominant role over the mixed layer. This suggests that if convective instabilities are well resolved in the surface layer at the onset, the overall representation of the CBL is expected to improve.

To extend conclusions from the analytic model to nonlinear CBL convection, reverse one-way nested simulations are performed. To ensure the quality of the simulated surface layer, an LES run is upscaled to the gray-zone grid and used to drive nested gray-zone simulations. Consistent with the predictions of the analytic model, simulation results show improvements compared to the stand-alone gray-zone run, in terms of the timing for the onset of convection, as well as the convective structures for the overall CBL. The nested simulations also reveal some deficiencies of the analytic model, which is the complete decoupling of momentum and potential temperature in the assumed neutrally stratified mixed layer. A result of this deficiency is the underprediction of $\langle \overline{w'w'} \rangle$ in the nested run above the surface layer (Fig. 6). The underprediction is reduced in the actual two-way nested simulations in a separate paper, when the nonlinear feedback from the mixed layer to the surface layer is allowed. Model sensitivity to the nest-layer depth is also tested. Results show that when nested up to half the boundary layer depth, overall agreement between the nest and the filtered LES run is achieved both within and outside the nest region. Higher nest levels only show small improvements, which are mostly manifested in high-order statistics.

Overall, the analytic model and the one-way nested tests show that unlike small surface-layer eddies that

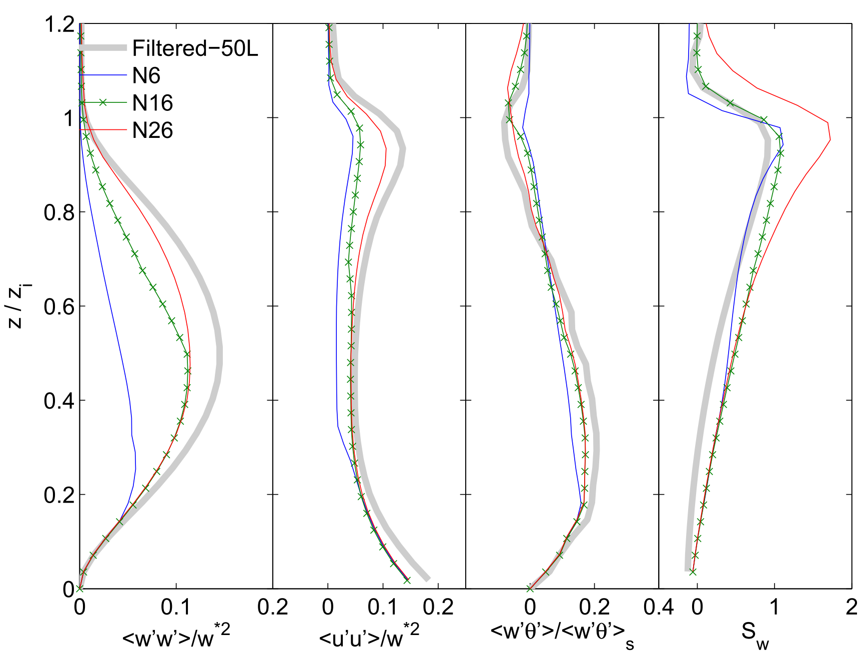


FIG. 12. As in Fig. 6, but for two additional runs with higher nest levels. Note that the 950G-50L run is renamed N6 for ease of comparison. Note the different $x$ axis limits compared to Fig. 6.

tend to stay within the surface layer (Sullivan et al. 1996), organized convection that originates from the surface layer does propagate upward and sets the convective structures for the rest of the CBL. The coupling between the surface layer and the rest of the CBL in terms of organized convection is a surface-layer-dominated one. The dynamics of the surface layer has a strong influence on that of the mixed layer, although some feedback exists as revealed by the vertical velocity variance. The conclusions suggest that a better representation of the unstable surface layer can improve the overall simulation of the CBL at gray-zone resolutions.

*Acknowledgments.* We are grateful to Prof. Tina Chow for reviewing an initial draft of the manuscript. We gratefully acknowledge the High Performance Computing Center (HPCC) of Nanjing University for doing the numerical calculations in this paper on its IBM Blade cluster system. All authors were supported by the Research 973 Program of China (2013CB430103). Bowen Zhou was further supported by the Dengfeng Program of Nanjing University, the National Natural Science Foundation of China (Grant 41505047), and a collaborative project on PBL parameterizations with the Beijing Urban Meteorology Institute. Kefeng Zhu is also supported by the Foundation of China Meteorological Administration (Grant GYHY201506006) and the National Science Foundation of China (Grant 41405100).

## REFERENCES

Arakawa, A., and C.-M. Wu, 2013: A unified representation of deep moist convection in numerical modeling of the atmosphere. Part I. *J. Atmos. Sci.*, **70**, 1977–1992, doi:10.1175/JAS-D-12-0330.1.

——, J. H. Jung, and C. M. Wu, 2011: Toward unification of the multiscale modeling of the atmosphere. *Atmos. Chem. Phys.*, **11**, 3731–3742, doi:10.5194/acp-11-3731-2011.

Boutle, I. A., J. E. J. Eyre, and A. P. Lock, 2014: Seamless stratocumulus simulation across the turbulent gray zone. *Mon. Wea. Rev.*, **142**, 1655–1668, doi:10.1175/MWR-D-13-00229.1.

Ching, J., R. Rotunno, M. LeMone, A. Martilli, B. Kosovic, P. A. Jimenez, and J. Dudhia, 2014: Convectively induced secondary circulations in fine-grid mesoscale numerical weather prediction models. *Mon. Wea. Rev.*, **142**, 3284–3302, doi:10.1175/MWR-D-13-00318.1.

Clarke, R. H., A. J. Dyer, R. R. Brook, D. G. Reid, and A. J. Troup, 1971: The Wangara experiment: Boundary layer data. CSIRO Division of Meteorological Physics Tech. Paper 19, 340 pp.

Deardorff, J., 1974: Three-dimensional numerical study of the height and mean structure of a heated planetary boundary layer. *Bound.-Layer Meteor.*, **7**, 81–106, doi:10.1007/BF00224974.

Drazin, P. G., and W. H. Reid, 2004: *Hydrodynamic Stability.* Cambridge University Press, 628 pp.

Efstathiou, G. A., R. J. Beare, S. Osborne, and A. P. Lock, 2016: Grey zone simulations of the morning convective boundary layer development. *J. Geophys. Res. Atmos.*, **121**, 4769–4782, doi:10.1002/2016JD024860.

Gentine, P., G. Bellon, and C. C. van Heerwaarden, 2015: A closer look at boundary layer inversion in large-eddy simulations and bulk models: Buoyancy-driven case. *J. Atmos. Sci.*, **72**, 728–749, doi:10.1175/JAS-D-13-0377.1.

Gibbs, J. A., E. Fedorovich, and A. M. J. van Eijk, 2011: Evaluating Weather Research and Forecasting (WRF) Model predictions of turbulent flow parameters in a dry convective boundary layer. *J. Appl. Meteor. Climatol.*, **50**, 2429–2444, doi:10.1175/2011JAMC2661.1.

Holtslag, A. M., and C.-H. Moeng, 1991: Eddy diffusivity and countergradient transport in the convective atmospheric boundary layer. *J. Atmos. Sci.*, **48**, 1690–1698, doi:10.1175/1520-0469(1991)048<1690:EDACTI>2.0.CO;2.

Hong, S.-Y., Y. Noh, and J. Dudhia, 2006: A new vertical diffusion package with an explicit treatment of entrainment processes. *Mon. Wea. Rev.*, **134**, 2318–2341, doi:10.1175/MWR3199.1.

Honnert, R., V. Masson, and F. Couvreux, 2011: A diagnostic for evaluating the representation of turbulence in atmospheric models at the kilometric scale. *J. Atmos. Sci.*, **68**, 3112–3131, doi:10.1175/JAS-D-11-061.1.

Hunt, J. C. R., J. C. Kaimal, and J. E. Gaynor, 1988: Eddy structure in the convective boundary layer—New measurements and new concepts. *Quart. J. Roy. Meteor. Soc.*, **114**, 827–858, doi:10.1002/qj.49711448202.

Ito, J., H. Niino, M. Nakanishi, and C.-H. Moeng, 2015: An extension of the Mellor–Yamada model to the terra incognita zone for dry convective mixed layers in the free convection regime. *Bound.-Layer Meteor.*, **157**, 23–43, doi:10.1007/s10546-015-0045-5.

Kaimal, J. C., and J. J. Finnigan, 1994: *Atmospheric Boundary Layer Flows: Their Structure and Measurement.* Oxford University Press, 289 pp.

Klemp, J. B., and R. B. Wilhelmson, 1978: The simulation of three-dimensional convective storm dynamics. *J. Atmos. Sci.*, **35**, 1070–1096, doi:10.1175/1520-0469(1978)035<1070:TSOTDC>2.0.CO;2.

LeMone, M. A., F. Chen, M. Tewari, J. Dudhia, B. Geerts, Q. Miao, R. L. Coulter, and R. L. Grossman, 2010: Simulating the IHOP_2002 Fair-Weather CBL with the WRF-ARW–Noah modeling system. Part I: Surface fluxes and CBL structure and evolution along the eastern track. *Mon. Wea. Rev.*, **138**, 722–744, doi:10.1175/2009MWR3003.1.

Lenschow, D. H., and B. B. Stankov, 1986: Length scales in the convective boundary layer. *J. Atmos. Sci.*, **43**, 1198–1209, doi:10.1175/1520-0469(1986)043<1198:LSITCB>2.0.CO;2.

Lock, A. P., A. R. Brown, M. R. Bush, G. M. Martin, and R. N. B. Smith, 2000: A new boundary layer mixing scheme. Part I: Scheme description and single-column model tests. *Mon. Wea. Rev.*, **128**, 3187–3199, doi:10.1175/1520-0493(2000)128<3187:ANBLMS>2.0.CO;2.

Malavelle, F. F., J. M. Haywood, P. R. Field, A. A. Hill, S. J. Abel, A. P. Lock, B. J. Shipway, and K. McBeath, 2014: A method to represent subgrid-scale updraft velocity in kilometer-scale models: Implication for aerosol activation. *J. Geophys. Res. Atmos.*, **119**, 4149–4173, doi:10.1002/2013JD021218.

Mirocha, J., G. Kirkil, E. Bou-Zeid, F. K. Chow, and B. Kosović, 2013: Transition and equilibration of neutral atmospheric boundary layer flow in one-way nested large-eddy simulations using the Weather Research and Forecasting Model. *Mon. Wea. Rev.*, **141**, 918–940, doi:10.1175/MWR-D-11-00263.1.

Muñoz-Esparza, D., B. Kosović, J. Mirocha, and J. van Beeck, 2014: Bridging the transition from mesoscale to microscale turbulence in numerical weather prediction models. *Bound.-Layer Meteor.*, **153**, 409–440, doi:10.1007/s10546-014-9956-9.

——, J. K. Lundquist, J. A. Sauer, B. Kosović, and R. R. Linn, 2017: Coupled mesoscale-LES modeling of a diurnal cycle during the CWEX-13 field campaign: From weather to boundary-layer eddies. *J. Adv. Model. Earth Syst.*, **9**, 1572–1594, doi:10.1002/2017MS000960.

Nakanishi, M., and H. Niino, 2009: Development of an improved turbulence closure model for the atmospheric boundary layer. *J. Meteor. Soc. Japan*, **87**, 895–912, doi:10.2151/jmsj.87.895.

Newsom, R. K., and R. M. Banta, 2003: Shear-flow instability in the stable nocturnal boundary layer as observed by Doppler lidar during CASES-99. *J. Atmos. Sci.*, **60**, 16–33, doi:10.1175/1520-0469(2003)060<0016:SFIITS>2.0.CO;2.

Piotrowski, Z. P., P. K. Smolarkiewicz, S. P. Malinowski, and A. A. Wyszogrodzki, 2009: On numerical realizability of thermal convection. *J. Comput. Phys.*, **228**, 6268–6290, doi:10.1016/j.jcp.2009.05.023.

Salesky, S. T., M. Chamecki, and E. Bou-Zeid, 2017: On the nature of the transition between roll and cellular organization in the convective boundary layer. *Bound.-Layer Meteor.*, **163**, 41–68, doi:10.1007/s10546-016-0220-3.

Shin, H. H., and S.-Y. Hong, 2013: Analysis of resolved and parameterized vertical transports in convective boundary layers at gray-zone resolutions. *J. Atmos. Sci.*, **70**, 3248–3261, doi:10.1175/JAS-D-12-0290.1.

——, and ——, 2015: Representation of the subgrid-scale turbulent transport in convective boundary layers at gray-zone resolutions. *Mon. Wea. Rev.*, **143**, 250–271, doi:10.1175/MWR-D-14-00116.1.

Skamarock, W. C., 2004: Evaluating mesoscale NWP models using kinetic energy spectra. *Mon. Wea. Rev.*, **132**, 3019–3032, doi:10.1175/MWR2830.1.

Stull, R. B., 1988: *An Introduction to Boundary Layer Meteorology*. Kluwer Academic Publishers, 666 pp.

Sullivan, P. P., and E. G. Patton, 2011: The effect of mesh resolution on convective boundary layer statistics and structures generated by large-eddy simulation. *J. Atmos. Sci.*, **68**, 2395–2415, doi:10.1175/JAS-D-10-05010.1.

——, J. C. McWilliams, and C. H. Moeng, 1996: A grid nesting method for large-eddy simulation of planetary boundary-layer flows. *Bound.-Layer Meteor.*, **80**, 167–202, doi:10.1007/BF00119016.

Sun, W. Y., and C. Z. Chang, 1986: Diffusion model for a convective layer. Part I: Numerical simulation of convective boundary layer. *J. Climate Appl. Meteor.*, **25**, 1445–1453, doi:10.1175/1520-0450(1986)025<1445:DMFACL>2.0.CO;2.

Thurston, W., R. J. B. Fawcett, K. J. Tory, and J. D. Kepert, 2016: Simulating boundary-layer rolls with a numerical weather prediction model. *Quart. J. Roy. Meteor. Soc.*, **142**, 211–223, doi:10.1002/qj.2646.

Tong, C., J. C. Wyngaard, S. Khanna, and J. G. Brasseur, 1998: Resolvable- and subgrid-scale measurement in the atmospheric surface layer: Technique and issues. *J. Atmos. Sci.*, **55**, 3114–3126, doi:10.1175/1520-0469(1998)055<3114:RASSMI>2.0.CO;2.

Warner, T. T., R. A. Peterson, and R. E. Treadon, 1997: A tutorial on lateral boundary conditions as a basic and potentially serious limitation to regional numerical weather prediction. *Bull. Amer. Meteor. Soc.*, **78**, 2599–2617, doi:10.1175/1520-0477(1997)078<2599:ATOLBC>2.0.CO;2.

Wyngaard, J. C., 2004: Toward numerical modeling in the "terra incognita." *J. Atmos. Sci.*, **61**, 1816–1826, doi:10.1175/1520-0469(2004)061<1816:TNMITT>2.0.CO;2.

Xue, M., J. Zong, and K. K. Droegemeier, 1996: Parameterization of PBL turbulence in a multi-scale nonhydrostatic model. Preprints, *11th Conf. on Numerical Weather Prediction*, Norfolk, VA, Amer. Meteor. Soc., 363–365.

——, K. K. Droegemeier, and V. Wong, 2000: The Advanced Regional Prediction System (ARPS)—A multi-scale nonhydrostatic atmospheric simulation and prediction model. Part I: Model dynamics and verification. *Meteor. Atmos. Phys.*, **75**, 161–193, doi:10.1007/s007030070003.

——, and Coauthors, 2001: The Advanced Regional Prediction System (ARPS)—A multi-scale nonhydrostatic atmospheric simulation and prediction tool. Part II: Model physics and applications. *Meteor. Atmos. Phys.*, **76**, 143–165, doi:10.1007/s007030170027.

——, F. Kong, K. W. Thomas, J. Gao, Y. Wang, K. Brewster, and K. K. Droegemeier, 2013: Prediction of convective storms at convection-resolving 1 km resolution over continental United States with radar data assimilation: An example case of 26 May 2008 and precipitation forecasts from spring 2009. *Adv. Meteor.*, **2013**, 259052, doi:10.1155/2013/259052.

Yamada, T., and G. Mellor, 1975: Simulation of Wangara atmospheric boundary layer data. *J. Atmos. Sci.*, **32**, 2309–2329, doi:10.1175/1520-0469(1975)032<2309:ASOTWA>2.0.CO;2.

Zhou, B., J. S. Simon, and F. K. Chow, 2014: The convective boundary layer in the terra incognita. *J. Atmos. Sci.*, **71**, 2545–2563, doi:10.1175/JAS-D-13-0356.1.